Hot electron collection on brookite nanorods lateral facets for plasmon-enhanced water oxidation

Alberto Naldoni,[†] Tiziano Montini,[#] Francesco Malara,[†] Marta M. Mróz,[§] Alessandro Beltram,[#] Tersilla Virgili,[§] Chiara L. Boldrini,[†] Marcello Marelli,[†] Ismael Romero-Ocaña,[#] Juan José Delgado Jaén,[‡] Vladimiro Dal Santo*,[†] Paolo Fornasiero*,[#]

[†] CNR – Istituto di Scienze e Tecnologie Molecolari, Via C. Golgi 19, 20133, Milano, Italy

[#] Dipartimento di Scienze Chimiche e Farmaceutiche e Unita di Ricerca ICCOM-CNR Trieste, INSTM Trieste, Università degli Studi di Trieste, Via L. Giorgieri 1, 34127 Trieste, Italy

[§] CNR - Istituto di Fotonica e Nanotecnologie (IFN), Dipartimento di Fisica, Politecnico di Milano, Piazza Leonardo Da Vinci, 32 20133 Milano, Italy

[‡] Departamento de Ciencia de los Materiales e Ingeniería Metalúrgica y Química Inorgánica, Facultad de Ciencias, Universidad de Cádiz, Campus Río San Pedro, 11510, Puerto Real, Cádiz, Spain

Supporting Information Placeholder

ABSTRACT: Photocatalytic reactions could enhance the share of chemicals produced through renewable sources. The efficiency of photocatalysts drastically depends on light absorption, on surface energy of the crystals, and on the properties of nano-building blocks assembled in devices. Here, we show that photoelectrochemical water oxidation on brookite TiO_2 nanorods is greatly enhanced by engineering the location of Au nanoparticles deposition. Brookite photoanodes show a very low onset potential for water oxidation to H_2O_2 of -0.2 V_{RHE} due to energetics of exposed crystal facets. By combining electrochemical measurements and ultrafast optical spectroscopy, we link the water oxidation activity with electron-hole recombination phenomena. The preferential Au decoration at the electrode/water interface produces highly enhanced photocurrent, while when Au is distributed along the whole film thickness the activity is depressed with respect to pure brookite. In the latter case, Au nanoparticles act as recombination centers with plasmonic carriers recombining on the same timescale of their generation (fs). Conversely, Au surface decoration enables hot electrons lifetime 4 orders of magnitude longer (ns) due to efficient hopping on brookite lateral facets thus providing an efficient path for plasmon-enhanced solar water oxidation.

INTRODUCTION

Photoelectrochemical (PEC) water splitting is a promising key enabling technology to boost future H_2-based economy, combining the use of a natural and abundant primary energy source (solar light) and a renewable, abundant, and cheap raw material (H_2O) for the production of a sustainable fuel (H_2).[1,2] Titanium dioxide (TiO_2) materials have been extensively investigated as photoanodes for water oxidation in PEC cells because of their favorable band-edge positions, superior chemical stability, low material cost and abundance.[3–6] Despite anatase and rutile are the most frequently investigated forms of TiO_2, brookite is a promising material for increasing the performances of photo(electro)chemical devices because of its peculiar structural and electronic properties.[7,8] Thanks to its more positive energy of conduction band, brookite demonstrated high activity in H_2 production by photore-

forming of oxygenated compounds and ammonia oxidation.[9–11] Despite some favorable characteristics, the performance of brookite are still far from those required for the application in PEC devices, mainly because of fast recombination of photogenerated electron-hole pairs and poor response under visible light.

Electron-hole pair lifetime can be increased by engineering the crystal shape of TiO_2 particles. Shape-controlled TiO_2 nanocrystal are able to accumulate electrons and holes on different crystal facets.[12–15] The synthesis of nanocrystals with desired shapes and exposed facets, well established for anatase phase, has been reported only marginally for brookite.[10,16–19] Therefore, the control of its morphology opens new possibilities on the exploitation of this metastable polymorph.

On the other hand, metal/TiO_2 composites absorption can be extended to visible and near-infrared wavelengths by using plasmonic nanoparticles (NPs). Localized surface plasmon resonance (LSPR) refers to the collective oscillation of surface electrons in metal nanostructures in response to an external alternating electric field such as solar light. The decay of surface plasmons produces highly energetic (hot) electrons,[20–22] that offer unique reaction pathways and enhanced solar absorption to increase chemical reactions yield. For instance, plasmon-enhanced photocatalysis has shown great potential in selective oxidations, C-C couplings, pollutants removal, solar cells, and PEC water splitting.[21–36] However, the lifetime of hot electrons is typically on the timescale of hundreds of fs,[35–38] while chemical reactions proceed much slower (i.e., ms to s). Hot electron injection into the conduction of TiO_2 across the interfacial Schottky barrier allows the stabilization of plasmonic charges and their use in catalysis. Nevertheless, the use of shape-controlled nanocrystals and nanostructured films, produced by their ordered assembly, may induce a further order of magnitude increase in hot carriers' lifetime and thus an increased photocatalytic activity. The spatial distribution of the plasmonic component with respect to the semiconductor is one of the key design aspects of more efficient solar-to-fuels (and -electricity) devices. This geometry-dependent plasmonic enhancement has been thoroughly investigated only in the case of solar cells.[39] In contrast with photovoltaics, during water oxidation, increased generation of charge carriers are particularly significant only at the semiconductor-liquid junction, where the catalytic reactions

occur. Reports on this matter for PEC water splitting have been quite elusive and works on embedded and surface plasmonic decoration have shown controversial results.[30,32,40]

Herein we show that brookite TiO_2 nanorods with well-developed crystal facets present unprecedented low onset potential and high photocurrent during selective water oxidation to hydrogen peroxide, with concomitant H_2 production at the cathode. Through a precise control of Au NPs deposition on brookite nanorods lateral facets, we clearly show that bulk versus surface plasmonic decoration generates dramatically different PEC activity. When Au NPs were homogeneously dispersed in the whole film thickness of brookite nanocrystals, photocurrent was depressed if compared to bare TiO_2. Conversely, if Au was preferentially deposited close to the electrode/water interface, we observed strongly enhanced photocurrent and four orders of magnitude slower hot electrons decay time.

EXPERIMENTAL METHODS

Synthesis of TiO_2 brookite nanorods. TiO_2 brookite nanorods were synthesized by a hydrothermal method as previous reported by some of us.[9] Briefly, 1.5 mL of aqueous solution of titanium(IV) bis (ammonium lactate) dihydroxyde (50 wt%, from Sigma-Aldrich) was mixed with 13.5 mL of 7.0 M urea aqueous solution. The obtained solution was treated hydrothermally in a 40 mL Teflon-lined autoclave at 160 °C for 24 h. After recovering of the solid product and washing with distilled water for several times, the material was calcined at 400 °C for 3 h in air to remove all the residual organic contaminants.

Preparation of TiO_2-based electrodes. Titania pastes were prepared following the procedure described by Seigo Ito et al.[41] Dried TiO_2 powder was dispersed in ethanol, treated in an ultrasonic bath for 30 min, and then stirred at 50 °C for 1 h. This procedure was repeated three times in order to obtain a homogeneous and opalescent colloidal suspension. The latter was mixed with ethylcellulose previously dissolved in ethanol (10 wt %) and stirred again at 50 °C overnight. Terpineol was added and the resulting mixture was further stirred for 6 h. Finally, ethanol was removed using a rotary evaporator to obtain pastes with suitable viscosity. The TiO_2 pastes had the following weight percentage composition: TiO_2: 12%; ethylcellulose: 6%; terpineol: 82%. The pastes were spinned on FTO/glass substrate at different rates: 1500 rpm for 15 s, 2500 rpm for 120 s and 3500 rpm for 120 s. The spinning procedure was repeated 5 times for each electrode. After each deposition, the electrodes were heated at 150 °C for 15 min followed by the final sintering at 450 °C for 1 h, to remove the organic material and to promote linking and interaction between the nanorods.

Assembly of TiO_2/Au electrodes. Au NPs were deposited on TiO_2 nanorods' lateral facets through photodeposition (125 W Hg lamp) using $HAuCl_4$ (1 wt% Au/TiO_2 ratio) in ethanol solution at 20 °C for 3 h. Au-decorated TiO_2 nanorods were then spin-coated on FTO glass to produce TiO_2/Au bulk samples. TiO_2/Au-surface samples were produced through Au photodeposition on TiO_2 electrodes already spinned. Photodeposition was performed in a PEC cell using a three-electrode configuration at open circuit voltage dipping the electrodes in a $HAuCl_4$ 0.3 mM ethanol solution and irradiating for different times under 1 Sun illumination (100 mW/cm^2).

Material Characterizations. Powder X-Ray Diffraction patterns were acquired in the range $10° < 2\theta < 100°$ using a Philips X'Pert diffractometer using a monochromatized Cu Kα ($\lambda = 0.154$ nm) X-ray source. Data were analyzed using the PowderCell 2.0 software. Preferential growth of the brookite nanorods was taken into account in the Rietveld analysis. Mean crystallite sizes were calculated applying the Scherrer equation to the principal reflections. Raman spectra were collected using a inVia Renishaw mi-

crospectrometer equipped with a Nd:YAG laser using an excitation wavelength of 532 nm. Preparation of the samples was carried out via drop casting the dispersed particles onto silicon wafers. N_2 physisorption measurements at the liquid nitrogen temperature were performed on the powders scratched from the prepared films using a Micrometrics ASAP 2020 automatic analyzer. The samples were degassed in vacuum at 120 °C for 12 h prior to analysis. Diffuse reflectance UV-vis spectroscopy was performed with a Thermo Scientific Evolution 600 spectrophotometer, equipped with a diffuse reflectance accessory Praying–Mantis sampling kit (Harrick Scientific Products, USA). Energy-dispersive X-ray line scan analysis (EDX; EDAX Sirion 200/400) on cross sections of Au-decorated TiO_2 electrodes were performed with a XL30 environmental scanning electron microscopy (ESEM-FEG Philips) under high vacuum condition at 25 keV. The morphology of the composite materials was investigated by high resolution TEM (HR-TEM) measurements, performed on a TEM JEOL 2010-FEG microscope with an acceleration voltage of 200 kV and with 0.19 nm spatial resolution at Scherzer defocus conditions. In order to obtain accurate particle size distribution of the Au NPs, High-Angle Annular Dark-Field (HAADF) – Scanning Transmission Electron Microscopy (STEM) technique was carried out using an electron probe of 0.5 nm and a diffraction camera length of 120 cm. The size distribution of Au NPs deposited on TiO_2 was calculated by measuring the dimension of 400 particles through HAADF-STEM images. High resolution HAADF-STEM images were performed on a Titan Themis instrument using a camera length of 10 cm. Gold loading was measured with an Inductively Coupled Plasma/Optical Emission Spectrometer ICP-OES (ThermoScientific iCAP6300Duo) by external calibration. Thin films were digested in a crucible at RT with 3 mL of aqua regia solution for 3 h and diluted with milliQ water.

Electrochemical characterizations. The electrodes were electrochemically characterized in a three-electrode system: the reference electrode was an Ag/AgCl electrode, while a high surface area Pt mesh was the counter electrode. The potential (E) was referred to the reversible hydrogen electrode (RHE) scaled through the Nernst equation:

$$E_{RHE} = E_{AgCl} + 0.197\,V + 0.059\,pH \qquad (1)$$

where E_{AgCl} is the measured electrode potential *vs*. the used reference electrode and 0.197 V is the reference electrode standard potential vs. the normal hydrogen electrode. Below, all measurements will be reported with respect to RHE. PEC measurements were carried out in 1 M NaOH aqueous solution (pH 13.6). Linear sweep voltammetry curves were measured at a scan rate of 10 mV/s.

PEC measurements were made with a PGSTAT204 Autolab potentiostat. The electrolyte was degassed with inert gas (N_2 or Ar) prior carrying out any PEC measurements. 300 W xenon arc lamp (calibrated at 100 mW/cm^2) was used as light source. Detection of reaction products were performed during chronoamperometric experiments at 1.23 V under irradiation. Gaseous products were stripped from the PEC cell by an Ar flow (30 mL min^{-1}) and detected by GC analysis using an Agilent 7890 equipped with a RT-Msieve 5A column (30 m x 0.52 mm ID) using Ar as carrier and connected to a TCD. H_2O_2 concentration in the solution at the end of chronoamperometric PEC experiments was determined by $KMnO_4$ colorimetric test.[42,43] 2.00 mL of solution from the PEC experiment were mixed with 2.00 mL of H_2SO_4 4M and 50 μL of $KMnO_4$ 0.01 M (previously standardized using $Na_2C_2O_4$). The concentration of residual MnO_4^- was determined using an UV-vis spectrophotometer (SHIMADZU, UV-2450), recording absorbance at 525 nm. H_2O_2 concentration has

been calculated from the decrease of MnO_4^- concentration with respect to black analysis (using initial NaOH solution) on the basis of the following reaction:

$$6H^+ + 2MnO_4^- + 5H_2O_2 \rightarrow 2Mn^{2+} + 8H_2O + 5O_2 \qquad (2)$$
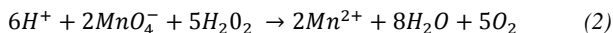
Blank experiments without illumination and application of external bias confirm the absence of interfering processes.

Electrochemical Impedance Spectroscopy measurements were performed using 10 mV amplitude perturbation at frequency between 0.01 Hz and 1 MHz. The data were fitted by Randles circuit by means of Z-View® software (Scribner Associated Incorporated). Mott-Schottky analysis were performed in dark at the follow frequencies: 10 Hz, 1 kHz and 1 MHz. The incident photon to current efficiency (IPCE) measurements were carried out by applying a set of band-pass filters (fwhm 40 nm, wavelength range 400−850 nm, Thorlabs) at the light source. At least three electrodes of each type were fabricated and tested. We fabricated and tested 3-5 electrodes of each type and the photocurrent values fell in a ±10% range from reported value.

Ultrafast optical pump and probe experiments. Femtosecond pump-probe measurements were carried out by using a laser system based on a Ti:Sapphire (Libra, Coherent), delivering pulses at 1-kHz repetition rate with 780-nm center wavelength, 150-fs duration. The beam was then split into the pump and the probe. Two different pump wavelengths were employed: (i) for the pure brookite, the pump beam was focused on a beta-barium borate (BBO) crystal for the second harmonic generation (390 nm); (ii) for the films containing Au NPs, an optical parametric amplifier (OPA) was used to center the pump wavelength at 520 nm. The probe was focused on a sapphire plate (1-mm thick) to generate a white light continuum (WLC) (470-770 nm). Pump and probe pulses were spatially overlapped on the sample, and a computer-controlled delay stage was used to control the delay between them. The evolution of the differential transmission measurements was recorded over the whole visible spectrum using a fast optical multichannel analyzer (OMA) as a detection system. All measurements were performed in air, the pump pulse power was 0.3 mW/pulse for Au-containing films and 0.45 mW/pulse for bare brookite.
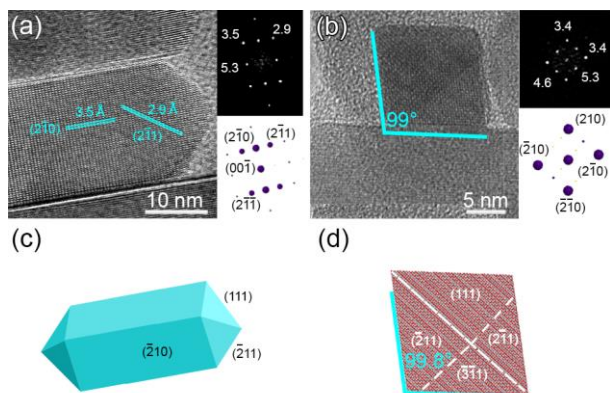

Figure 1. HR-TEM images, Digital Diffraction Pattern (DDP), and simulated diffraction patterns in kinematic conditions along the <120> (a) and <001> (b) directions of brookite nanorods. (c,d) Model of the nanorods obtained from the HR-TEM images of different nanorods in different orientation. The cross section of the nanorod (b) is included to show that the exposed lateral facets correspond to the (210) and equivalent family of planes.

RESULTS AND DISCUSSION

X-ray powder diffraction pattern of the brookite nanorods can be indexed as pure brookite TiO_2 with an orthorhombic structure (space group *Pbca*). Cell parameters, calculated from the Rietveld analysis, were in excellent agreement with the theoretical values (Figure S1 and Table S1).[44] Notably, the effect of preferential growth along the *c* axis must be taken into account to obtain the best goodness of the fit. The Raman spectrum of the calcined sample (Figure S2) shows the presence of the bands typical of brookite including A_{1g} (129, 153, 196, 248, 414, 546, 639 cm^{-1}), B_{1g} (214, 287, 331, 451, 612 cm^{-1}), B_{2g} (258, 368, 394, 463, 585 cm^{-1}) and B_{3g} (248, 322, 503 cm^{-1}). The good agreement of the observed Raman bands with the active modes of brookite reported previously,[45] together with the absence of the strong band at 516 cm^{-1} (characteristic of anatase) confirmed that the final powder was pure brookite TiO_2.[19]

A bandgap of 3.3 eV for brookite nanorods was measured using diffuse reflectance UV-Vis spectroscopy (Figure S3). This value is larger than that of rutile and anatase polymorphs, and in agreement with previous reports.[7,10,11]

N_2 physisorption analysis showed a Type IV isotherm, typical of mesoporous materials, with H3 type hysteresis, indicative of slit-shaped pores (Figure S4a).[46] The surface area of the material, calculated following the BET method, was 36 m^2 g^{-1}. BJH analysis, performed on the desorption branch on the isotherm (Figure S4b), showed a maximum in the pore size distribution around 32 nm and a cumulative pore volume of 0.386 mL g^{-1}.

Representative TEM micrographs (Figure 1 and S5) showed that brookite nanocrystals grew as nanorods with length of 60-130 nm and width of 20-40 nm. HR-TEM and HAADF analysis evidenced that the nanorods are elongated along the [001] direction, preferentially exposing facets belonging to the {210} family on the lateral facets.

Figure 1 shows representative HR-TEM images of the nanorods along different directions and the corresponding digital diffraction patterns. From these images, it is possible to recognize the high degree of crystallinity of the synthesized nanorods and their rhombohedral section. The pyramid forming the tip of the nanorods is not perfectly symmetric exposing several unusual facets with high indexes such as {$\bar{2}11$} and {$\bar{3}\bar{1}1$} beyond the more common {111} facets (Figures 1 and S5). Additional univocal interpreted HR-TEM images of brookite nanorods with different orientations are presented in Figure S5, to confirm the statistical relevance of the exposed facets.

We took advantage of brookite nanorods building blocks to assemble plasmonic photoanodes for water oxidation. Bare brookite electrode was used as reference material. Five subsequent spin-coating deposition cycles were necessary to obtain high PEC activity and a final film thickness of ~2 μm (Figure S6). The temperature used to consolidate the TiO_2 film after the spin-coating deposition (450 °C) did not affect the phase composition of TiO_2, as the brookite was thermally stable at least up to 650 °C.[44,47]

Two electrode configurations containing Au NPs in different location along the film thickness were prepared (Figure 2): a) homogeneously distributed in the whole film (TiO_2/Au-bulk) or selectively deposited at the surface of the film (TiO_2/Au-surface).

TiO_2/Au-bulk was prepared (Figure 2a) by first photodepositing Au NPs on brookite nanorods and then preparing a viscous paste that was finally spin-coated on FTO-coated glass slides and calcined at 450 °C for 1 h to remove organic binders. Differently, TiO_2/Au-surface configuration was prepared (Figure 2b) by preparation of TiO_2 nanorods film, followed by Au photodeposition in a PEC cell by using a three electrodes configuration at open circuit voltage. The Au loading has been optimized by measuring the
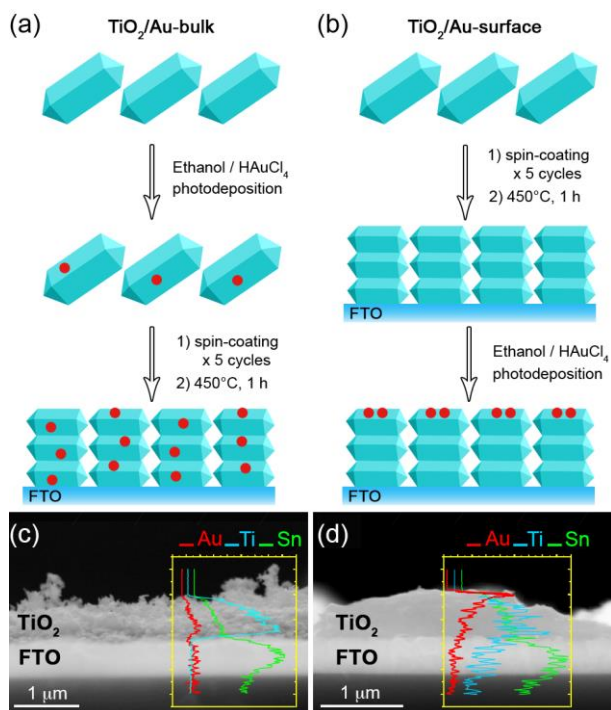
Figure 2. Cartoons representing the processes adopted to build the final electrodes configuration: (a) TiO$_2$/Au-bulk and (b) TiO$_2$/Au-surface (30 min photodeposition). Representative cross section SEM images and EDX line scan analysis of (c) TiO$_2$/Au-bulk and (d) TiO$_2$/Au-surface.

photocurrent after photodeposition of Au for different irradiation time. Photocurrent shows a progressive increase with Au loading, reaching a plateau above 30 min of irradiation (Figure S7). It is reasonable that, at very high loading, Au can completely cover the TiO$_2$ surface thus changing the nature of the photoanode leading to a decrease of the photocurrent.[33,48–52] However, under our experimental conditions, despite the increase in Au loadings, we did not observe any decrease in photocurrent up to 60 min of irradiation, suggesting that significantly longer photodeposition treatments are needed to appreciate this phenomenon. Therefore, we decided to proceed with our investigation using the material prepared by photodeposition of Au for 30 min, that is the sample showing the highest photocurrent with the lower Au loading.

Cross section SEM images of the prepared films (Figures 2 and S8) evidenced that a network among the brookite nanorods was obtained. EDX line scans collected along the section of the films (Figures 2c-d) showed that Sn was present only inside the FTO layer, while Ti was only in the TiO$_2$ film. As desired, Au distribution was completely different for the two configurations analyzed. Au signal in the TiO$_2$/Au-bulk material is very low, closed to the noise of the EDX detector. This is in agreement with the low Au content (3 wt%) and with the homogeneous distribution of Au NPs along the film thickness. Different is the situation of the TiO$_2$/Au-surface (30 min). In fact, ICP-OES analysis confirmed that the Au loading in TiO$_2$/Au-bulk was 5-fold that of the TiO$_2$/Au-surface sample. Nevertheless, thanks to the deposition technique employed, Au is concentrated on the outermost layer of the film. As a result, Au signal is very high and progressively decreases with depth of the film.

Au NPs size distributions obtained from HAADF-STEM analysis are shown in Figure 3a (TiO$_2$/Au-bulk) and 3b (TiO$_2$/Au-surface). Both configurations presented a high number of Au NPs having diameter below 5 nm, with average Au particle sizes of 2.8 nm and 2.2 nm for TiO$_2$/Au-bulk and TiO$_2$/Au-surface, respectively. However, both samples showed few Au NPs with diameter

exciding 10 nm and being at maximum 25 nm. This feature was more evident for TiO$_2$/Au-bulk (Figures S9-S10) probably due to the particles sintering due to the thermal treatment at 450 °C carried out to consolidate the film.

HAADF-STEM images of TiO$_2$/Au-bulk (Figures 3c and S9) and TiO$_2$/Au-surface (Figure 3d and S9) clearly demonstrated that small Au NPs (2-5 nm) selectively grew on the lateral facets of brookite TiO$_2$ nanorods (see arrows). Upon irradiation most of the photogenerated electrons excited in the brookite nanorods were collected on the {210} lateral facets, being then consumed in the reduction reaction of Au^{3+} to Au^0. Spatial separation of reduction and oxidation sites on different facets of brookite nanorods was already proved by tracking the distribution of photodeposited Pt and PbO$_2$.[17,53]
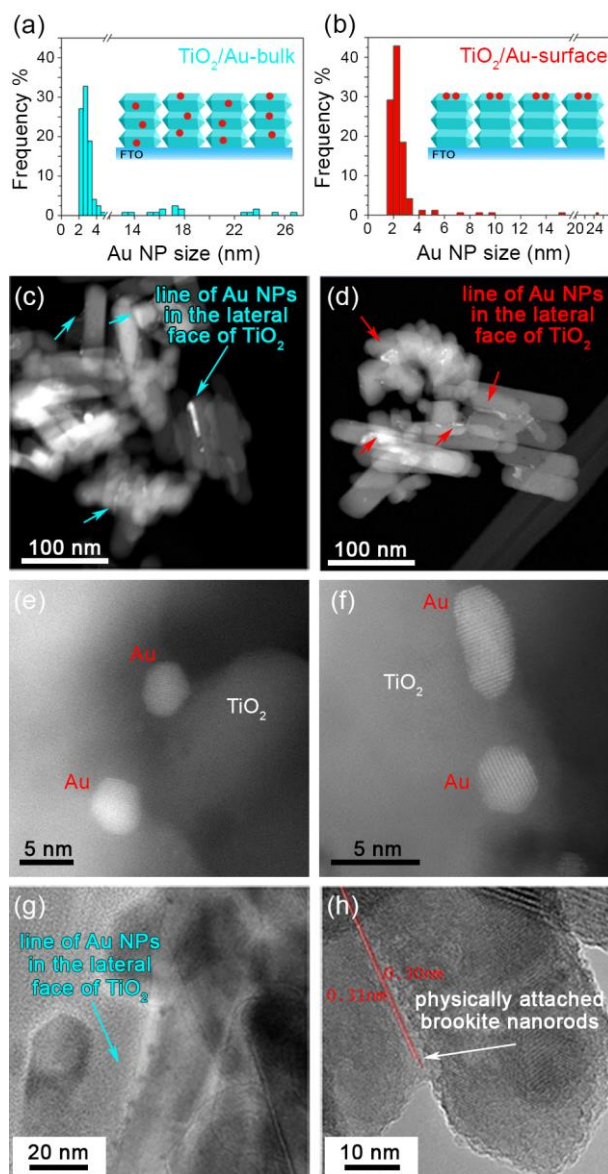

Figure 3. Au NPs size distribution for TiO$_2$-Au/bulk (a) and TiO$_2$-Au/surface. Approximately 400 Au NPs were counted. (b). Representative HAADF-STEM and HR-STEM micrographs showing the preferential deposition of Au NPs on the lateral facets of brookite nanorods both for TiO$_2$-Au/bulk (c and e, see blue arrows) and TiO$_2$-Au/surface (d and f, see red arrows). TEM images of brookite nanorods physically attached along their lateral facets (g: TiO$_2$-Au/bulk; h: TiO$_2$-Au/surface).

Interestingly, in some TiO$_2$ nanorods the {210} lateral facets were decorated with multiple Au NPs forming rows of plasmonic NPs perfectly aligned and well attached on the oxide surface (Figures 3 and S10). It is worth noting also that some nanorods were physically attached along the lateral facets and presented twin-like morphology. This might influence the charge migration inside the TiO$_2$ films and consequently the PEC performance of brookite-based photoanodes.

Figure 4a shows the photocurrent (J) curves for the investigated photoanodes. All electrodes were stable and showed constant generation of photocurrent (see Figure S11). Pure brookite TiO$_2$ reaches a plateau photocurrent of about 0.148 mA cm^{-2} at 1.23 V (all the potential hereafter are referred to RHE). The bulk and surface Au decoration induced opposite effects: TiO$_2$/Au-bulk resulted in ~30% reduction of J (0.101 mA cm^{-2}), while TiO$_2$/Au-surface produced a 70% enhancement (0.253 mA cm^{-2}).

Both TiO$_2$/Au-bulk and TiO$_2$/Au-surface showed the typical gold anodic oxidation peak around 1 V (in NaOH 1M) that yielded an Au(III) hydroxide surface layer, according to the following reaction:[54,55]

$$Au \cdot H_2O + 3\,OH^- \rightarrow Au(OH)_3 + H_2O + 3\,e^- \qquad (3)$$
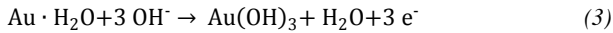
The electrochemical active Au, obtained from the integrated area of the peak at 1 V, was significantly affected by the preparation procedure: the electrochemical active Au in the TiO$_2$/Au-surface is 3-fold of that of TiO$_2$/Au-bulk, despite the 5-fold higher metal loading in the latter case observed by ICP-OES. This data is clearly consistent with the Au NPs size distribution obtained from

TEM investigation (Figure 3) and the fact that the consecutive annealing steps in the preparation of TiO$_2$/Au-bulk favored the sintering of Au NPs and their embedding between adjacent brookite nanorods, thus resulting in sites not accessible to the electrolyte.

It is interesting to observe that brookite electrodes, with or without Au NPs, showed a very low onset potential for water oxidation (E$_{onset}$ ~ -0.2 V). E$_{onset}$ of our electrodes is among the best reported, comparable with values obtained for reduced anatase nanowires and TiO$_2$/CdSe heterostructure.[56,57] Density functional theory calculations revealed that the conduction band of brookite lies at a more cathodic potential than those of anatase and rutile,[8,19] providing a higher thermodynamic driving force for the H$_2$ evolution processes.[7,9,10] The distinct atomic arrangements characteristic of the lateral and apical facets of brookite TiO$_2$ crystal result in different surface energy levels of the conduction and valence bands.[19,53] This distinctive feature drives the electrons to the lateral {210} facets and holes to the apical {111}/{$\bar{2}$11}/{$\bar{3}\bar{1}$1} facets, respectively, leading to efficient charge separation.[17] In addition, reactants adsorption/desorption ability is strongly facets-dependent.[53,58]

All these brookite nanorods properties act synergistically to produce the onset potential of -0.2 V observed for our electrodes. This is probably ascribable to the good balance between exposed lateral facets {210} and apical facets {111}/{$\bar{2}$11}/{$\bar{3}\bar{1}$1} that induced a low charge transfer resistance both at the electrode/electrolyte interface and along the film thickness.
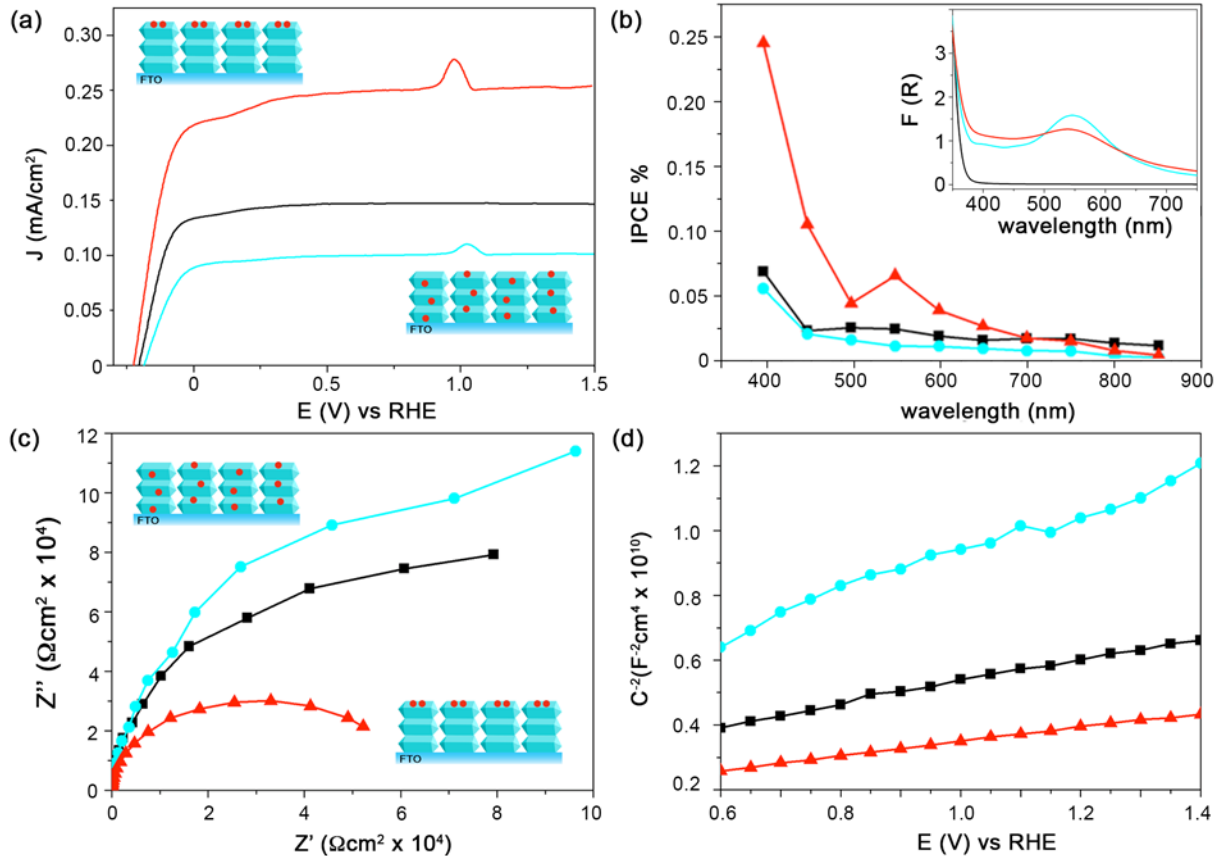

Figure 4. Electrochemical characterizations and absorption spectra of brookite TiO$_2$ (black curves), TiO$_2$/Au-bulk (blue curves), and TiO$_2$/Au-surface (red curves). (a) Linear sweep voltammetry under 1 Sun illumination scanning from cathodic to anodic potentials. (b) IPCE measured at 1.23 V vs RHE and absorption spectra of TiO$_2$-based samples (inset). (c) EIS analysis carried out at 1.23 V vs RHE under 1 Sun illumination. (d) Mott-Schottky analysis performed in dark conditions.
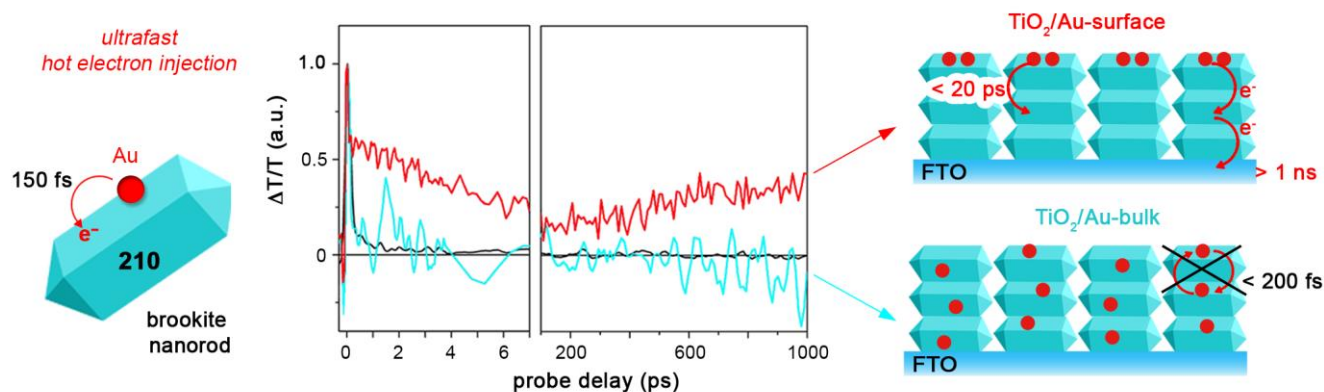
Figure 5. Time profiles of transient absorption at 690 nm for TiO_2 (black curve), TiO_2/Au-bulk (blue curve) and TiO_2/Au-surface (red curve) films. The wavelength of excitation for the bare TiO_2 was 390 nm, while for TiO_2/Au films was 550 nm.

To detect the products of the PEC process, on-line GC analysis has been performed stripping the gaseous products with an Ar flow from a PEC cell working with TiO_2/Au-surface photoanode. No significant amount of products was observed simply applying 1.23V between the working and the counter electrode. After switching on the light source, a significant increase in photocurrent is observed, reaching a stable value of 0.240 mA/cm^2 in a few minutes (Figure S12a). At the same time, H_2 evolution is detected by GC analysis. Its concentration in the gas stream increased during the first hour while it progressively decreased, becoming negligible after 4h of irradiation of the photoanode (Figure S12b). Notably, the amount of O_2 detected in the gas stream was below the detection limit of the analytic instrument employed during the overall duration of the test. Analysis of the solution collected after the 8h experiment presented in Figure S12 with the KMnO$_4$ colorimetric test revealed the formation of H_2O_2, measuring a final concentration of 8.21 x 10^{-5} M, correspondent to the formation of 3.28 μmol of H_2O_2. This value well agrees with the overall H_2 amount of 3.38 μmol calculated by integration of the profile obtained by GC analysis (Figure S12b). No other reaction products were detected. These results clearly indicated that the process taking place in our PEC cell is:

$$2H_2O \rightarrow H_2 + H_2O_2 \qquad (4)$$

H_2O_2 is a high value-added and green oxidation reagent, interesting in view of its use in H_2O_2 fuel cells,[59,60] catalytic selective oxidations of organic substrates,[61] environmental purification and antibacterial applications.[62] To the best of our knowledge, only few other recent reports have highlighted this possibility, however without foreseeing high selectivty.[63–66]

Despite this, the observed amount of H_2 and H_2O_2 are much lower than that expected on the basis of the electrical current measured (36 μmol). The low apparent faradaic efficiency for both H_2 and H_2O_2 calculated on the basis of this results (around 9%) and the relatively fast decrease in H_2 production observed (Figure S12b) are ascribable to the design of our PEC cell where the H_2O_2 produced at the photoanode is decomposed by reduction at the Pt counter electrode, therefore competing with H_2 production.

Incident photon-to-current efficiency (IPCE) curves (Figure 4b) show that TiO_2/Au-surface had higher efficiencies at all wavelengths with respect of both TiO_2 and TiO_2/Au-bulk, in agreement with J-E measurements. In particular, TiO_2/Au-surface showed a pronounced IPCE peak around 550 nm, which corresponds to the LSPR absorption peak (inset Figure 4b), proving that plasmonic

hot electron collection was one of the reasons underling the increased PEC activity.[67–69] Hot electrons were injected across the Schottky barrier and collected into the conduction band of TiO_2, while hot holes could actively participate to oxidation processes at the electrode/water interface (Figure S13).[67,70] Interestingly, no beneficial effect of the presence of Au was observed in the IPCE profile of TiO_2-Au/bulk even if an intense LSPR peak was present in its absorption spectra (Figure 4b, inset). The Au NPs in TiO_2/Au-surface produced enhanced IPCE also at wavelengths < 500 nm. Two main effects drove this behavior. First, the Au/TiO_2 junctions are not-ideal Schottky diodes and electrons from Au interband transitions (i.e., cold electrons), absorbing around 450-500 nm, are collected due to nanoscale inhomogeneities, interface structural effect and edge-induced tunneling effect.[71–73] Secondly, the IPCE curve showed a significant enhancement at 400 nm with probably even higher increase in the UV region. The photocurrent signal in this spectral region is directly related to the TiO_2 band gap electron-hole separation efficiency and Au NPs preferentially deposited at the electrode-electrolyte interface passivated surface traps thus increasing both open-circuit voltage and photocurrent.[33,74,75]

To provide more insights on the structure-activity relationships of brookite-based photoanodes, electrochemical impedance spectroscopy (EIS) measurements under 1 Sun irradiation at 1.23 V was carried out (Figure 4c). At this potential J-E and EIS curves were not affected by Au oxidation peak and the arcs could be ascribable to the electrical bulk behavior.[74,76] The presence of Au along the entire bulk of the TiO_2 electrode (TiO_2-Au/bulk) induced a higher electron-hole recombination (i.e., a larger impedance arc) and thus a lower photocurrent if compared to bare TiO_2. These results suggested that, in TiO_2-Au/bulk electrode, Au NPs acted as recombination centers. Conversely, the highest water oxidation activity of TiO_2-Au/surface was due to the reduced recombination of photogenerated charge carriers across the electrode (i.e., a smaller impedance arc). The selective surface deposition of Au NPs generates the ideal nanoarchitecture for hot electron collection that resulted in highly plasmon-enhanced photocurrent.

Mott-Schottky plots (Figure 4d) present a positive slope indicating that the brookite forming our electrodes is a n-type semiconductor. Table S2 summarizes the main parameters extrapolated by Mott-Schottky measurements. The flat band potential (E_{fb}) of bare brookite photoanodes was -0.6 V. Bulk or surface Au-functionalization produced negligible changes on E_{fb} (±40 mV). The donor density (N_D) concentration for the reference brookite nanorods electrode was 4.27 x 10^{20} cm^{-3}, while TiO_2-Au/bulk and TiO_2-Au/surface showed a -34% and +6% variation on N_D, re-

spectively (Table S2). The higher is the donor density, the higher is the charge concentration at the TiO$_2$/water interface. This in principle produces an increased band bending in the semiconductor driving a better separation of photogenerated charges and thus a higher water oxidation activity. In our case, the Au-surface decoration did not change significantly N_D and the interface properties. Conversely, the Au-bulk configuration changed both the overall resistive and capacitive properties of the brookite photoelectrode, resulting in scarce performance.

To further understand the different PEC efficiency observed for TiO$_2$/Au-bulk and TiO$_2$/Au-surface, hot electron dynamics was analyzed by using fs ultrafast pump-probe spectroscopy.[77] Figure S14 shows the transient absorption spectra at different probe delay times for pure brookite TiO$_2$, TiO$_2$/Au-bulk, and TiO$_2$/Au-surface films. Both Au-containing films revealed a strong photoinduced absorption signal due to Au LSPR excitation, while the TiO$_2$ electrode did not present significant variations in the investigated wavelengths range.

After LSPR excitation, Landau damping produces hot electron-hole pairs on the timescale of few tens of fs.[22] The semiconductor/metal interface drives the ultrafast injection (about 240 fs) of hot electrons into the semiconductor conduction band.[78] Depending whether these charges accumulate at the surface or in the bulk (free electrons) of the nanocrystal, a characteristic transient absorption is generated mainly in the visible or in the mid-infrared region, respectively.[79] We focused on the signal due to the surface contribution since (i) PEC water oxidation is a surface process and (ii) surface charge trapping drives efficiency in photocatalytic reactions.

Bare TiO$_2$ film was excited at a wavelength of 390 nm, just above the band gap energy of brookite. After pump excitation, a photoinduced absorption signal due to surface trapped charges (holes and electrons) was detected at around 690 nm.[80] The decay was very fast occurring in less than 200 fs (Figure 5, black line).

When we excited the plasmonic photoanodes with pump wavelength resonant to LSPR peak (i.e., λ_{ex} = 550 nm), both TiO$_2$/Au-bulk and TiO$_2$/Au-surface (see Figure 5, blue and red line, respectively) showed a photoinduced absorption signal at 690 nm. At this wavelength, brookite nanorods do not absorb (i.e., charge generation form band gap transitions are not activated), with the new signals deriving from transfer of hot electrons from Au NPs to brookite nanorods (see also Figure S13).

Hot electron injection occurred in ~150 fs (Figure 5), in agreement with previous reports.[78] Most importantly, in TiO$_2$/Au-bulk all excited carriers recombined in few hundreds of fs, the same timescale of plasmonic injection.[79]

TiO$_2$/Au-bulk has been assembled starting from brookite nanorods having Au NPs already deposited before the electrode preparation. This produced a thin film with homogeneous Au distribution along the whole thickness (Figure 2c). Microscopically, this means that some adjacent TiO$_2$ nanorods had Au NPs on parallel facets. Therefore, after hot electron injection from Au NPs to one TiO$_2$ lateral facets, electrons may encounter another Au NPs on the same lateral facet or on the lateral facet of an adjacent nanorod. Not only TiO$_2$/Au-bulk configuration did not produce plasmon-enhanced photocurrent (Figure 4a), but Au NPs at nanorods boundaries act as recombination centers for electrons traveling toward the FTO contact thus reducing the overall photocurrent.

Conversely, in the case of TiO$_2$/Au-surface, we detected two and four orders magnitude longer charge decay times, namely, < 20 ps and > 1 ns. Only some electrons recombined instantaneously, i.e. in less than 200 fs. TiO$_2$/Au-surface presented a high Au concentration solely at the electrode/water interface (Figure 2d). After plasmonic injection into the superficial TiO$_2$ layer, the electrons took different time to reach other nanorods depending on the distance between the donor and acceptor. Then, the injected electrons could be gradually transferred back to the oxidized Au NPs

with the two different decay times (< 200 fs and ≈ 10 ps) or go more inside in the bulk creating the very slow rising time of ≈ 500 ps.[81] This latter recombination evidenced the ability of electrons to be efficiently transferred across the brookite electrodes through a hopping mechanism involving the {210} facets of brookite nanorods (Figure 5). When Au was preferentially deposited close to the electrode/water interface (TiO$_2$/Au-surface), the plasmonic sensitization was effective providing extra charges for water oxidation and thus producing greatly enhanced photocurrent.

CONCLUSION

We have shown that brookite TiO$_2$ nanorods are promising building blocks to obtain highly efficient photoanodes for PEC water splitting. Brookite nanorods with well-developed crystal facets provided optimal charge carrier separation and tailored redox potentials that resulted in favorable onset potential (-0.2 V_{RHE}) for the water oxidation, producing H$_2$O$_2$ at the photoanode and H$_2$ at the Pt cathode. This finding promotes brookite as interesting materials for production of in situ H$_2$O$_2$ solutions to be used in fuel cells, in selective oxidation reactions (in tandem with adequate catalysts) and in other relevant environmental applications. Furthermore, through selective Au nanoparticles deposition on particular crystal facets, we demonstrated the importance of plasmonic geometry on PEC activity. When Au nanoparticles were distributed along the whole TiO$_2$ film thickness, they acted mainly as recombination centers for charge carriers and depressed the overall photocurrent. Otherwise, if the plasmonic decoration was preferentially at the surface of the film, the photocurrent was strongly enhanced. This configuration allowed to extend the lifetime of injected hot electrons to the timescale of ps and ns. {210} lateral facets sustained the hopping of photogenerated hot electrons through the assembled nanorods thus allowing the observation of these long-lived plasmonic charge carrier decay times. More generally, we have shown that nanocrystals with controlled shape and exposed crystal facets are fundamental building blocks to unravel important issues and for achieving increased performances in photoelectrochemical solar energy conversion.

ASSOCIATED CONTENT

Supporting Information

Additional material characterizations. This material is available free of charge via the Internet at http://pubs.acs.org.

AUTHOR INFORMATION

Corresponding Author

v.dalsanto@istm.cnr.it , pfornasiero@units.it

Notes
The authors declare no competing financial interests.

REFERENCES

(1) Armaroli, N.; Balzani, V. *ChemSusChem* **2011**, *4*, 21–36.

(2) Bowker, M. *Green Chem.* **2011**, *13*, 2235–2246.

(3) Cappelletti, G.; Ardizzone, S.; Bianchi, C. L.; Gialanella, S.; Naldoni, A.; Pirola, C.; Ragaini, V. *Nanoscale Res. Lett.* **2009**, *4*, 97–105.

(4) Chen, X.; Shen, S.; Guo, L.; Mao, S. S. *Chem. Rev.* **2010**, *110*, 6503–6570.

(5) Grätzel, M. *Nature* **2001**, *414*, 338–344.

(6) Bak, T.; Nowotny, J.; Rekas, M.; Sorrell, C. . *Int. J. Hydrogen Energy* **2002**, *27*, 991–1022.

(7) Paola, A. Di; Bellardita, M.; Palmisano, L. *Catalysts* **2013**; *3*, 36-73.

(8) Angelis, F. De; Valentin, C. Di; Fantacci, S.; Vittadini, A.; Selloni, A. *Chem. Rev.* **2014**, *114*, 9708−9753.

(9) Beltram, A.; Romero-Ocana, I.; Delgado Jaen, J. J.; Montini, T.; Fornasiero, P. *Appl. Catal. A Gen.* **2016**, *518*, 167–175.

(10) Cargnello, M.; Montini, T.; Smolin, S. Y.; Priebe, J. B.; Delgado Jaén, J. J.; Doan-Nguyen, V. V. T.; McKay, I. S.; Schwalbe, J. A.; Pohl, M.-M.; Gordon, T. R.; Lu, Y.; Baxter, J. B.; Brückner, A.; Fornasiero, P.; Murray, C. B. *Proc. Natl. Acad. Sci.* USA **2016**, *113*, 3966–3971.

(11) Altomare, M.; Dozzi, M. V.; Chiarello, G. L.; Di Paola, A.; Palmisano, L.; Selli, E. *Catal. Today* **2015**, *252*, 184–189.

(12) Arienzo, M. D.; Dozzi, M. V.; Redaelli, M.; Credico, B. Di; Morazzoni, F.; Scotti, R.; Polizzi, S. *J. Phys. Chem. C* **2015**, *119*, 12385−12393.

(13) Liu, Y.; Liu, S.; He, D.; Li, N.; Ji, Y.; Zheng, Z.; Luo, F.; Liu, S.; Shi, Z.; Hu, C. *J. Am. Chem. Soc.* **2015**, *137*, 12697–12703.

(14) Roeffaers, M. B. J.; Sels, B. F.; Uji-I, H.; De Schryver, F. C.; Jacobs, P. A.; De Vos, D. E.; Hofkens, J. *Nature* **2006**, *439*, 572–575.

(15) Gordon, T. R.; Cargnello, M.; Paik, T.; Mangolini, F.; Weber, R. T.; Fornasiero, P.; Murray, C. B. *J. Am. Chem. Soc.* **2012**, *134*, 6751−6761.

(16) Buonsanti, R.; Grillo, V.; Carlino, E.; Giannini, C.; Kipp, T.; Cingolani, R.; Cozzoli, P. D. *J. Am. Chem. Soc.* **2008**, *130*, 11223–11233.

(17) Lin, H.; Li, L.; Zhao, M.; Huang, X.; Chen, X.; Li, G.; Yu, R. *J. Am. Chem. Soc.* **2012**, *134*, 8328–8331.

(18) Xu, Y.; Lin, H.; Li, L.; Huang, X.; Li, G. *J. Mater. Chem. A* **2015**, *3*, 22361–22368.

(19) Zhao, M.; Xu, H.; Chen, H.; Ouyang, S.; Umezawa, N.; Wang, D.; Ye, J. *J. Mater. Chem. A* **2015**, *3*, 2331–2337.

(20) Marimuthu, A.; Zhang, J.; Linic, S. *Science* **2013**, *339*, 1590–1593.

(21) Naldoni, A.; Riboni, F.; Guler, U.; Boltasseva, A.; Shalaev, V. M.; Kildishev, A. V. *Nanophotonics* **2016**, *5*, 112–133.

(22) Brongersma, M. L.; Halas, N. J.; Nordlander, P. *Nat. Photonics* **2015**, *10*, 25–34.

(23) Christopher, P.; Xin, H.; Marimuthu, A.; Linic, S. *Nat. Mater.* **2012**, *11*, 1044–1050.

(24) Christopher, P.; Xin, H.; Linic, S. *Nat. Chem.* **2011**, *3*, 467–472.

(25) Huang, X.; Li, Y.; Chen, Y.; Zhou, H.; Duan, X.; Huang, Y. *Angew. Chemie - Int. Ed.* **2013**, *52*, 6063–6067.

(26) Sugano, Y.; Shiraishi, Y.; Tsukamoto, D.; Ichikawa, S.; Tanaka, S.; Hirai, T. *Angew. Chemie - Int. Ed.* **2013**, *52*, 5295–5299.

(27) Wang, F.; Li, C.; Chen, H.; Jiang, R.; Sun, D.; Li, Q.; Wang, J.; Yu, J. C.; Yan, C. *J. Am. Chem. Soc.* **2013**, *135*, 5588−5601.

(28) Zheng, Z.; Tachikawa, T.; Majima, T. *J. Am. Chem. Soc.* **2015**, *137*, 948–957.

(29) Atwater, H. A; Polman, A. *Nat. Mater.* **2010**, *9*, 205–213.

(30) Thimsen, E.; Le Formal, F.; Grätzel, M.; Warren, S. C. *Nano Lett.* **2011**, *11*, 35–43.

(31) Li, J.; Cushing, S. K.; Zheng, P.; Meng, F.; Chu, D.; Wu, N. *Nat. Commun.* **2013**, *4*, 2651.

(32) Thomann, I; Pinaud, B. a; Chen, Z.; Jaramillo, T. F.; Clemens, B. M.; Mark, L. *Nano Lett.* **2011**, *11*, 3440–3446.

(33) Pu, Y. C.; Wang, G.; Chang, K. Der; Ling, Y.; Lin, Y. K.; Fitzmorris, B. C.; Liu, C. M.; Lu, X.; Tong, Y.; Zhang, J. Z.; Hsu, Y. J.; Li, Y. *Nano Lett.* **2013**, *13*, 3817–3823.

(34) Mukherjee, S.; Libisch, F.; Large, N.; Neumann, O.; Brown, L. V; Cheng, J.; Lassiter, J. B.; Carter, E. A; Nordlander, P.; Halas, N. J. *Nano Lett.* **2012**, *13*, 240–247.

(35) Brongersma, M. L.; Halas, N. J.; Nordlander, P. *Nat. Photonics* **2015**, *10*, 25–34.

(36) Amidani, L.; Naldoni, A.; Malvestuto, M.; Marelli, M.; Glatzel, P.; Dal Santo, V.; Boscherini, F. *Angew. Chemie Int. Ed.* **2015**, *54*, 5413 –5416.

(37) Harutyunyan, H.; Martinson, A. B. F.; Rosenmann, D.; Khorashad, L. K.; Besteiro, L. V.; Govorov, A. O.; Wiederrecht, G. P. *Nat. Nanotechnol.* **2015**, *10*, 770–774.

(38) Govorov, A. O.; Zhang, H.; Gun'Ko, Y. K. *J. Phys. Chem. C* **2013**, *117*, 16616–16631.

(39) Ferry, V. E.; Munday, J. N.; Atwater, H. A. *Adv. Mater.* **2010**, *22*, 4794–4808.

(40) Zhan, Z.; An, J.; Zhang, H. *ACS Appl. Mater. Int.* **2014**, *6*, 1139–1144.

(41) Ito, S.; Chen, P.; Comte, P.; Nazeeruddin, M. K.; Liska, P.; Pechy, P.; Grätzel, M. *Prog. Photovolt Res. Appl.* **2007**, *15*, 603–612.

(42) Daskalaki, V. M.; Panagiotopoulou, P.; Kondarides, D. I. *Chem. Eng. J.* **2011**, *170*, 433–439.

(43) Kiassen, N. V.; Marchington, D.; Mcgowant, H. C. E. *Anal. Chem.* **1994**, *66*, 2921–2925.

(44) Kumar, S. G.; Rao, K. S. R. K. *Nanoscale* **2014**, *6*, 11574–11632.

(45) Iliev, M. N.; Hadjiev, V. G.; Litvinchuk, A. P. *Vib. Spectrosc.* **2013**, *64*, 148–152.

(46) Sing, K. S. W.; Everett, D. H.; Haul, R. A. W.; Moscou, L.; Pierotti, L. A.; Rouquerol, J.; Siemieniewska, T. *Pure Appl. Chem.* **1985**, *57*, 603–619.

(47) Wang, Y.; Durupthy, O.; Cassaignon, S.; Revel, R.; Jolivet, J. *ACS Appl. Mater. Interfaces* **2012**, *4*, 752–760.

(48) Al-Azri, Z. H. N.; Chen, W.-T.; Chan, A.; Jovic, V.; Ina, T.; Idriss, H.; Waterhouse, G. I. N. *J. Catal.* **2015**, *329*, 355–367.

(49) Chen, W.; Chan, A.; Sun-waterhouse, D.; Moriga, T.; Idriss, H.; Waterhouse, G. I. N. *J. Catal.* **2015**, *326*, 43–53.

(50) Jovic, V.; Al-Azri, Z. H. N.; Chen, W.-T.; Waterhouse, D.; Idriss, H.; Waterhouse, G. I. N. *Top. Catal.* **2013**, *56*, 1139–1151.

(51) Jovic, V.; Chen, W.-T.; Sun-Waterhouse, D.; Blackford, M. G.; Idriss, H.; Waterhouse, G. I. N. *J. Catal.* **2013**, *305*, 307–317.

(52) Murdoch, M.; Waterhouse, G. I. N.; Nadeem, M. A.; Metson, J. B.; Keane, M. A.; Howe, R. F.; Llorca, J.; Idriss, H. *Nat. Chem.* **2011**, *3*, 489–492.

(53) Yang, Z.; Wang, B.; Cui, H.; An, H.; Pan, Y.; Zhai, J. *J. Phys. Chem. C* **2015**, *119*, 16905−16912.

(54) Burke, L. D.; Nugent, P. F. *Gold Bull.* **1997**, *30*, 43–53.

(55) Juodkazis, K.; Juodkazyt, J.; Jasulaitien, V.; Lukinskas, A.; Šebeka, B. *Electrochem. commun.* **2000**, *2*, 503–507.

(56) Luo, J.; Ma, L.; He, T.; Ng, C. F.; Wang, S.; Sun, H.; Fan, H. J. *J. Phys. Chem. C* **2012**, *116*, 11956–11963.

(57) Wang, G.; Wang, H.; Ling, Y.; Tang, Y.; Yang, X.; Fitzmorris, R. C.; Wang, C.; Zhang, J. Z.; Li, Y. *Nano Lett.* **2011**, *11*, 3026–3033.

(58) Ohno, T.; Higo, T.; Murakami, N.; Saito, H.; Zhang, Q.; Yang, Y.; Tsubota, T. *Appl. Catal. B Environ.* **2014**, *152*–*153*, 309–316.

(59) Mase, K.; Yoneda, M.; Yamada, Y.; Fukuzumi, S. *ACS Energy Lett.* **2016**, *1*, 913–919.

(60) Mase, K.; Yoneda, M.; Yamada, Y.; Fukuzumi, S. *Nat. Commun.* **2016**, *7*, 11470.

(61) Guidotti, M.; Pirovano, C.; Ravasio, N.; Lázaro, B.; Fraile, J. M. J. M.; Mayoral, J. a. J. A.; Coq, B.; Galarneau, A.; Lazaro, B.; Fraile, J. M. J. M.; Mayoral, J. a. J. A.; Coq, B.; Galarneau, A. *Green Chem.* **2009**, *11*, 1421−1427.

(62) Sánchez-Quiles, D.; Tovar-Sánchez, A. *Environ. Sci. Technol.* **2014**, *48*, 9037–9042.

(63) Fuku, K.; Sayama, K. *Chem. Commun.* **2016**, *52*, 5406–5409.

(64) Shiraishi, Y.; Kanazawa, S.; Kofuji, Y.; Sakamoto, H.; Ichikawa, S.; Tanaka, S.; Hirai, T. *Angew. Chemie - Int. Ed.* **2014**, *53*, 13454–13459.

(65) Teranishi, M.; Naya, S. I.; Tada, H. *J. Am. Chem. Soc.* **2010**, *132*, 7850–7851.

(66) Viswanathan, V.; Hansen, H. A.; Nørskov, J. K. *J. Phys. Chem. Lett.* **2015**, *6*, 4224–4228.

(67) Warren, S. C.; Thimsen, E. *Energy Environ. Sci.* **2012**, *5*, 5133.

(68) Ingram, D. B.; Christopher, P.; Bauer, J. L.; Linic, S. *ACS Catal.* **2011**, *1*, 1441–1447.

(69) Kale, M. J.; Avanesian, T.; Christopher, P. *ACS Catal.* **2014**, *4*,

116–128.

(70)   Clavero, C. *Nat. Photonics* **2014**, *8*, 95–103.

(71)   Kraya, R.; Kraya, L. Y.; Bonnell, D. A. *Nano Lett.* **2010**, *10*, 1224–1228.

(72)   Lord, A. M.; Maffeis, T. G.; Kryvchenkova, O.; Cobley, R. J.; Kalna, K.; Kepaptsoglou, D. M. D.; Ramasse, Q. M.; Walton, A. S.; Ward, M. B.; Koeble, J.; Wilks, S. P.; Köble, J.; Wilks, S. P. *Nano Lett.* **2015**, *15*, 4248–4254.

(73)   Qin, W.; Hou, J.; Bonnell, D. A. *Nano Lett.* **2014**, *15*, 211−217.

(74)   Malara, F.; Minguzzi, A.; Marelli, M.; Morandi, S.; Psaro, R.; Dal Santo, V.; Naldoni, A. *ACS Catal.* **2015**, *5*, 5292–5300.

(75)   Malara, F.; Fabbri, F.; Marelli, M.; Naldoni, A. *ACS Catal.* **2016**, *6*, 3619–3628.

(76)   Sivula, K. *J. Phys. Chem. Lett.* **2013**, *4*, 1624–1633.

(77)   Wu, K.; Chen, J.; Mcbride, J. R.; Lian, T. *Science* **2015**, *349*, 632–635.

(78)   Furube, A.; Du, L.; Hara, K.; Katoh, R.; Tachiya, M. *J. Am. Chem. Soc.* **2007**, *129*, 14852–14853.

(79)   Du, L.; Furube, A.; Hara, K.; Katoh, R.; Tachiya, M. *J. Photochem. Photobiol. C Photochem. Rev.* **2013**, *15*, 21–30.

(80)   Tamaki, Y.; Furube, A.; Murai, M.; Hara, K.; Katoh, R.; Tachiya, M. *Phys. Chem. Chem. Phys.* **2007**, *9*, 1453.

(81)   Tian, Y.; Tatsuma, T. *J. Am. Chem. Soc.* **2005**, *127*, 7632–7637.